ADVANCED ENGINEERING MATERIALS

DOI: 10.1002/adem.201700139

Study of Interfacial Interactions in Physically Transient Soft Layered Structures: A Step toward Understanding Interfacial Bonding and Failure in Soft Degradable Structures**

By *Yuanfen Chen, Reihaneh Jamshidi, Wangyujue Hong, Nicole N. Hashemi* and *Reza Montazami**

Soft multilayer structures have broad applications in transient electronics. Strain-mismatch-induced fracture is key in achieving physical transiency. Here, swelling-mismatch-induced fragmentation of physically transient electrodes is studied. The fragment size of the electrode layer as a function of initial defect distribution is investigated. The average fragment size is predicted and verified by a combination of experimental and FEM analysis. It is found that only large defects initiate fragmentation; this concept can be used to control disintegration of physically transient electronics by means of materials and design, and can be extended to study transiency of soft multilayer structures.

1. Introduction

Multilayer structures consisting of dissimilar materials are pervasive, and have attracted considerable interest and attention, since they are relevant to diverse engineering applications including soft electronics, stimuli responsive morphing structures,[1] batteries,[2] supercapacitors,[3] sensors,[4] actuators,[5–7] and many others. Besides fracture caused by external forces, such as contact load,[8–10] cyclic load,[11,12] and impact,[13] failures of multilayer structures can result from strain mismatch of the constituent layers: problems include thermal expansion mismatch,[14] hydro swelling mismatch,[15] strain gradient caused by non-uniform electric field,[16,17] and many others.[18,19] The strain-mismatch-induced fracture could occur in the form of layer delamination, surface cracking, or combination of both, depending on the layers to diverse engineering applications including soterial properties. Extensive research has studied the strain-mismatch-induced failure of hard material multilayer structures, such as interfacial delamination of thermal barrier coatings (TBC),[20–26] thermal fatigue of transistors,[27] cracking of ceramic actuators,[16] and supercapacitor.[28] Fracture of hard coating printed on soft substrate has also received considerable interest. Lu and colleagues found that the failure of polymer-supported un-annealed nanocrystalline metal films was concomitant with grain growth, strain localization, and interfacial debonding.[18] In another study, they found that the failure mode of stiff islands on deformable substrate, either channeling cracks or debonding, depends on the island size and thickness.[19] However, strain-mismatch-induced fracture of soft multilayer thin films (soft coating sprayed or printed onto soft substrate) is rarely reported.[29–31]

Soft multilayer thin films are widely applied in transient electronics, and swelling-mismatch-induced fragmentation of the coating layer speeds up the re-dispersion/dissolution process. The initial flaw distribution (or pre-crack distribution) plays a key role in the fracture of the material, affecting the fracture strength, final fragment size, and fatigue life. In real applications, obtaining the initial defect distribution is not always possible. In addition, the distribution of flaw size and location in real cases could

[*] *Dr. R. Montazami, Y. Chen, R. Jamshidi, Dr. W. Hong, Dr. N. N. Hashemi*
Department of Mechanical Engineering, Iowa State University, Ames, 50011 Iowa, USA
E-mail: reza@iastate.edu
Dr. N. N. Hashemi, Dr. R. Montazami
Ames Laboratory, Department of Energy, Ames, 50011 Iowa, USA

[**] *Authors would like to thank Sarah Kreutner for her contribution to technical editing of this work. (Supporting Information is available online from Wiley Online Library or from the author).*

© 2017 WILEY-VCH Verlag GmbH & Co. KGaA, Weinheim

complicate the strength analysis. Some researchers have simulated brittle fracture with controlled pre-existing flaws, such as flaws with designed length and location,[32] or uniformly distributed flaws.[33] Other researchers predicted the fatigue life of bulk metals using equivalent initial flaw size (EIFS) distribution. The EIFS was obtained using either the back-extrapolation method,[34–38] or the Kitagawars predicted the f.[39,40] In some applications, such as multilayer thin films, the initial flaw distribution in the coating can be estimated if the substrate is transparent. Again, strength analysis is rather complicated with defect distribution in real coating, but a fragment size analysis of surface cracking based on real initial defect distribution is feasible. Surface spalling of coating from swelling strain mismatch is essential for the fast disintegration of physically transient electronics, and the fragment size will affect the subsequent redistribution into the fluid.[15] To the best of our knowledge, few studies have investigated how the actual initial defect distribution affects the fragment size of the material, especially the soft coating in multilayer thin films.[41–43] Controlled fragmentation is possible, if the relation between the initial defect distribution and the fragment size is well understood.

Stress and fracture analysis of soft multilayer thin films resulting from strain mismatch could be challenging because of the dynamic material properties of the substrate and coating. In our grouplmsh defect distr,[44] we investigated the interfacial stress of the physically transient soft multilayer thin films caused by swelling mismatch, incorporating the dynamic material property of the swelling substrate. Here, we have studied the fracturing of such soft multilayer thin films under similar conditions. Results are presented for a prototypical electrode (lithium titanate electrode active material printed on poly(vinyl alcohol) (PVA) substrate), whose coating could disintegrate, when the substrate swells beyond some limit in water.[15] The relationship between initial defect distribution and fragment size was investigated and confirmed. The method presented here could be applied to analyze strain-mismatch-induced fracture of soft multilayer thin films with dynamic material properties.

2. Result and Discussion

2.1. True Stress–Strain Curve of the Electrode Layer

True stress–strain curve of the electrode layer is necessary for simulation of crack propagation. To obtain the true stress–strain curve of the electrode layer, Hollomonary for simulation of Eq. 1) was applied; where σ_t and ε_t are the true stress and true strain, respectively, K is the strength coefficient, and n is the strain-hardening exponent.

$$\sigma_t = K\varepsilon_t^n \tag{1}$$

According to the Considère criterion,[45] the necking occurs when the true strain reaches the strain-hardening exponent. Then strain-hardening exponent, n, can be obtained from Equation 2. To make the stress curve, as deduced from Equation 1, to intersect the true stress–strain curve when necking initiate, the strength coefficient K is defined as in Equation 3:

$$n = \ln(1 + \varepsilon_e) \tag{2}$$

$$K = \frac{\sigma_e(1 + \varepsilon_e)}{[\ln(1 + \varepsilon_e)]^{\ln(1+\varepsilon_e)}} \tag{3}$$

where ε_e and σ_e are the nominal strain and normal stress at the initiation of necking, respectively.

The nominal stress–strain curves for the free-standing electrodes were obtained using a dynamic mechanical analyzer. Based on the nominal stress–strain data, Hollomon free-standing electrodes were obtained usine true stress–strain curve. The nominal stress–strain curves and the true stress–strain curve are shown in Figure 1a, where $n = 0.02882$ and $K = 0.06912$. True strain beyond 5% is extrapolated for studying the crack initiation. As shown by the plot, stress increases almost linearly with the true strain after necking.

To verify the true stress–strain curve in Figure 1a, the curve was applied in a FEM model to obtain the swelling induced strain of the electrode layer as a function of the PVA swelling strain, ε_s, then the simulation outcomes were compared and verified by the experimental result. In the simulation, the PVA substrate was set to swell up to 10%, and the corresponding strain of the electrode layer was recorded. For experimental result, the prototypical electrodes were immersed into water to measure the total strain in x-axis E11 of the electrode coating as a function of swelling strain. As shown in Figure 1b, the simulation and the experimental results agree. For $\varepsilon_s < 3\%$, the experimentally-obtained values of the electrode strain were found to be slightly lower than those obtained from simulation. This mismatch could be due to the slight inward bending of the electrode upon exposure to water. The agreement of the experimental and simulation results validates the true stress–strain curve of the electrode coating. The true stress–strain curve was applied in the FEM simulation discussed in the following section.

2.2. Surface Crack Predominated Failure

To characterize the fracturing of the electrode, a series of images of the electrode during submersion were taken and analyzed. As shown in Figure 2a, surface cracking was found to be the predominant fracture form of the prototypical electrode. When the PVA substrate swelled, cracks initiated from the pre-existing defects in the electrode layer. These cracks propagated and merged, resulting in small electrode pieces. The fragments are then re-dispersed in water when the PVA substrate was almost dissolved. No obvious interfacial delamination was observed. The predominant surface failure could be because of the relatively strong interfacial bonding

© 2017 WILEY-VCH Verlag GmbH & Co. KGaA, Weinheim
ADVANCED ENGINEERING MATERIALS 2017,
DOI: 10.1002/adem.201700139

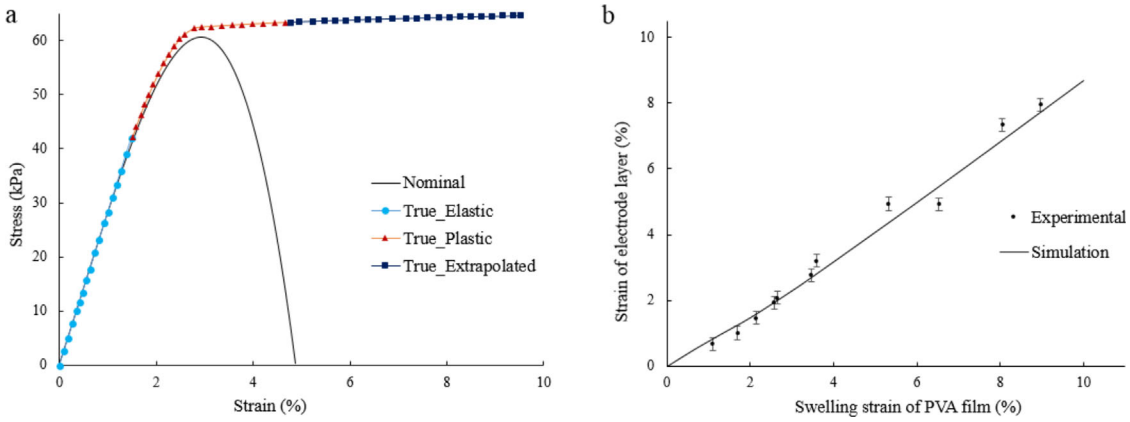

Fig. 1. (a) Nominal (experimentally obtained) and true (theoretically driven) stress–strain curves of the electrode coating; (b) swelling strain of the substrate and the resultant strain on the electrode layer (along the x-axis).

compared to that inside the electrode coating, as illustrated in Figure 2b. When the electrode slurry was sprayed onto the PVA substrate, the water solvent in the slurry wetted the surface of the PVA substrate. Once the multilayer thin film dried, exclusive bonding formed between the PVA substrate and the electrode's active material at the interface. PVA is also used as the binder insider the electrode layer, thus that the active material inside the electrode layer was also bonded by PVA. However, the concentration of PVA inside the electrode layer was much less compared to that at the interface; thus, the bonding inside the coating layer is weaker. As a result, spalling of the coating occurs instead of interfacial delamination.

2.3. Crack Propagation and the Resultant Fragmentation

The size of the electrode coating layer fragments that result from surface cracking affect the subsequent redistribution of the active electrode material into the fluid. The following sections will analyze the fragment size that results from the surface cracking and its dependency on the initial defect distribution.

Studies have demonstrated that the stress and energy required to initiate cracks from defects is inversely proportional to the defect length.[46–48] Griffith first reported that the maximum tension concentration at a crack tip is proportional to the square root of the length of the crack. On a later study, Rivlin and Thomas reported that the tearing energy at the incision of elastomer is proportional to the crack diameter. These findings suggest that larger defects require a smaller swelling strain to start propagate compared to smaller defects. To understand the correlation between the defect length and the critical swelling strain, straight-line, through-thickness defects with different lengths were simulated in ABAQUS using XFEM (extended finite element

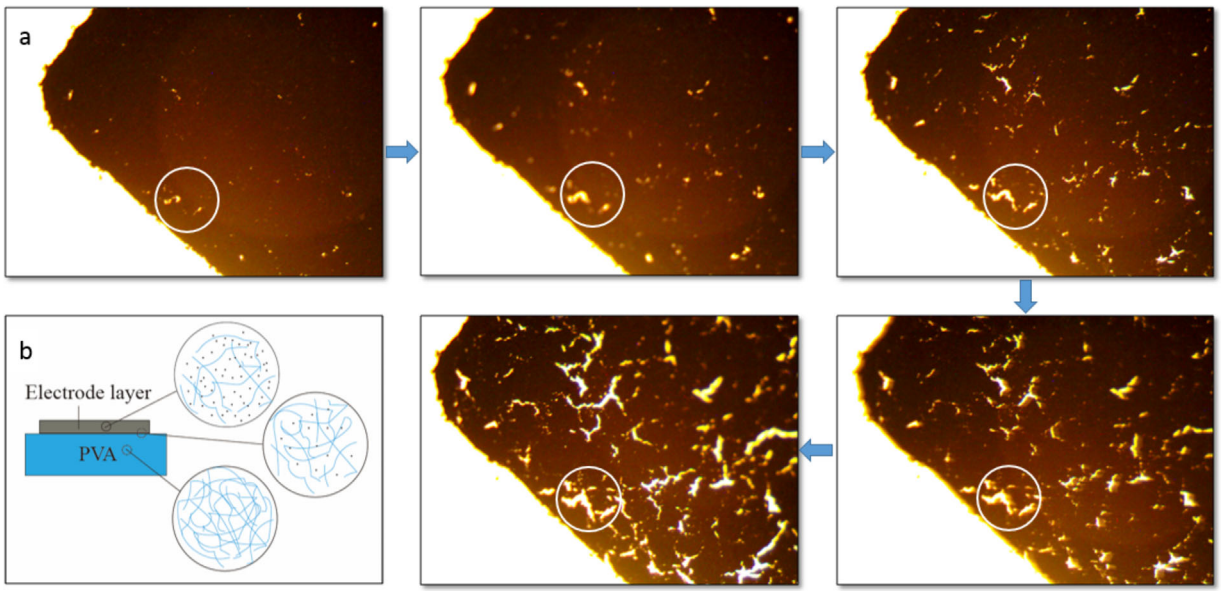

Fig. 2. (a) Series image showing the surface cracking of the electrode layer (images are taken at 10 s intervals). A few defects are circled to show the propagation of the initial defects. (b) Schematic showing the bonding inside and between electrode and PVA substrate.

DOI: 10.1002/adem.201700139
© 2017 WILEY-VCH Verlag GmbH & Co. KGaA, Weinheim

method). The simulated maximum principle strain and Von Mises stress for defects of 10 μm length at the moment the crack starts to propagate ($t = 0.00$ s) are presented in Figure 3a and b, respectively. Insets show magnified views of the crack and stress accumulation around the crack tip. This simulation aimed to gain insight on the general trend of critical swelling strain as a function of defect length. Figure 3c plots critical swelling strain as a function of defect length. The maximum defect length in the electrode coating was about 35 μm, which would start crack propagation at 5.86% of swelling strain. The critical swelling strain was almost identical for defect lengths ranging from 35 to 25 μm. As the defect length decreased, down to 10 μm, the critical swelling strain increased slowly. When the defect length decreased further, the critical swelling strain increased with a much sharper slope than before. Defects with length of 2.5 μm would start crack propagation at 12% of swelling strain. The critical swelling strain er, thct length curve (Figure 3c) appears to show that critical swelling strain for large defects is much smaller than for small defects. The experimental and simulation data suggest that as large defects propagate, they merge with small defects before small defects start to propagate independently. One large defect has one crack path, while small defects contribute to the zigzag pattern of the large defect crack path. Thus, the number of large defects define the number of fragments. Here, suggested by the experimental data, the large defects are defined as those longer than 5.5 μm, whose critical swelling strain for crack initiation is 1.5 times of the largest defect length's. The 5.5 μm threshold was obtained from the critical swelling strain – defect length curve. The large-defect-effect conclusion is verified in the following paragraph.

To confirm the large-defect-effect conclusion, the predicted average area of the fragments based on the large-defect-effect was compared with the actual average area. As shown in Figure 4a, images of the electrode coating were analyzed using MATLAB to get the number and length (maximum length) of the through-thickness defects. The number of defects longer than the 5.5 μm large-defect threshold was applied in calculation of the predicated average area. Large defects constitute approximately one third of the total number of defects. The calculation method and further details are provided in the supplementary document, Equation S1. Similarly, images of the fragments were analyzed to get their actual average area (Figure 4b,

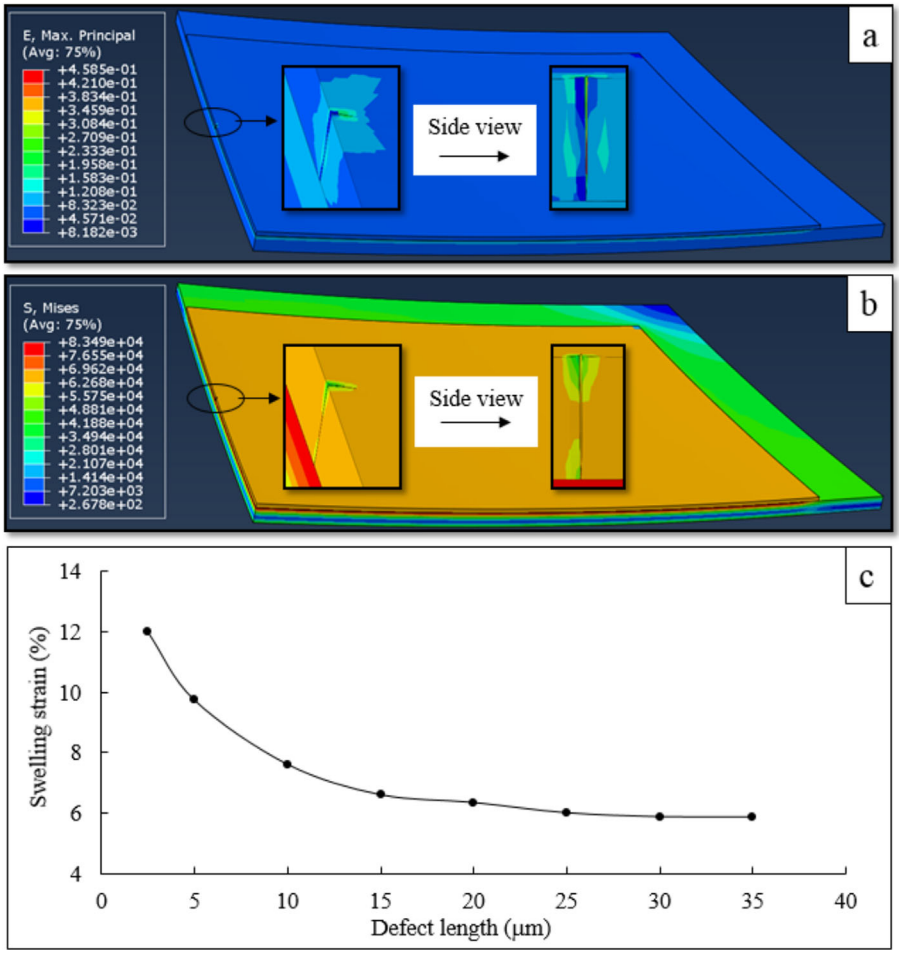

Fig. 3. (a) Maximum principle strain distribution through an electrode, with details shown around the crack; (b) Von Mises stress distribution, with details shown around the crack; (c) critical swelling strain – defect length curve.

© 2017 WILEY-VCH Verlag GmbH & Co. KGaA, Weinheim
ADVANCED ENGINEERING MATERIALS 2017,
DOI: 10.1002/adem.201700139

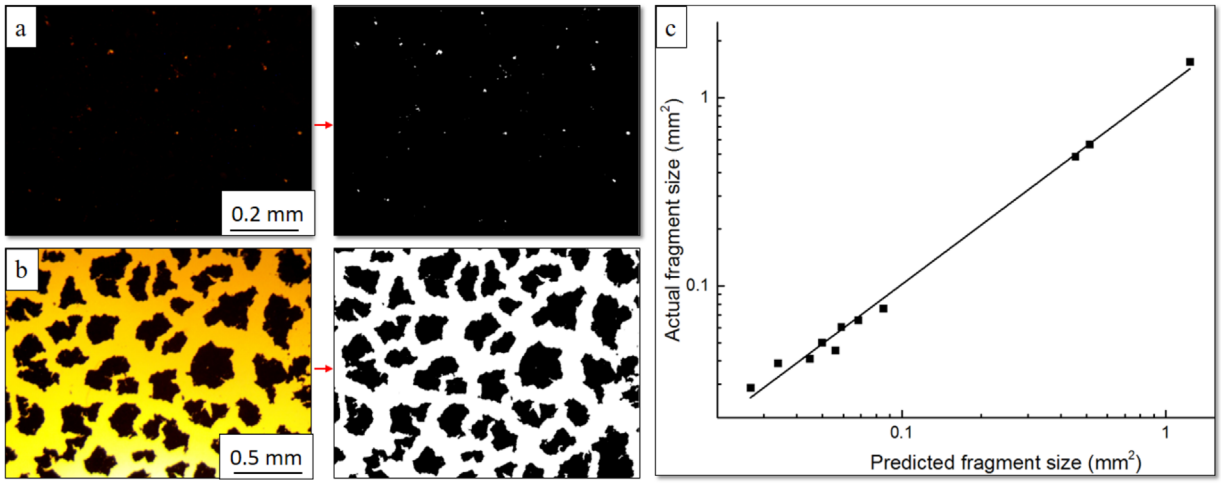

Fig. 4. (a) Image of typical defect distribution, before (left) and after (right) monochromic; (b) Image of typical fragments, before (left) and after (right) monochromic; (c) Predicted fragment area versus experimental fragment area.

Equation S2, and Figure S1). Figure 4a was taken at 10× magnification to estimate the defect length, while Figure 4b was taken at 4× magnification for a wider field of view. The comparison of the predicted average area and the actual average area is shown in Figure 4c; detailed data could be found in supporting document Table S1. Fragments with areas under 0.1 mm^2 are from very thin electrode layer, while areas above 0.4 mm^2 are from relatively thicker electrode layer. The linear fitting of the log-log data, using Origin, resulted in a slope value of 1.049, and an R-Square of 0.993. The linear relationship between the predicted average area and the actual average area supports the large-defect-effect that the number of large defects defines the number of fragments. Small defects merge during the propagation of large defects, so fragments have uneven edges. Fragment size is determined by the initial defect distribution, especially that of large defects.

3. Conclusion

Surface cracking is the predominant fracture form in the prototypical soft electronics. In this study, the correlation between the initial defect distribution and predictions of the fragment size in layered structures is established. The agreement of the predicted average fragment area and the actual average fragment area led to the "large-defect-effect" conclusion, suggesting that the number of large defects (length >5.5 μm) dictates the number of fragments, and therefore the average fragment area. Cracks initiate at large defects much earlier than at small defects; thus small defects typically merge into the propagating large defects, rather than initiating cracks independently. The conclusion that the preexisting characteristics of the layers can be used as a means to determine and control the mechanics of fragmentation of the layered structure as a whole, can be applied to design, tuning, and programming transiency and disintegration of printed layered soft electronics.

4. Experimental Section

4.1. Materials and Sample Preparation

Poly(vinyl alcohol)substrates with printed electrodes were fabricated according to our previous work.[15] Briefly, to fabricate substrates, PVA (Mw: 61 000 g mol^{-1}, 98.0–98.8% hydrolyzed, Sigma Aldrich) was used as received. One gram PVA, 0.1 g sucrose, and 50 μL of 1 M aqueous hydrochloric acid solution were added to 20 mL of DI (Deionized) water. The solution was then stirred at 70 °C for 4 h, cooled down to ambient temperature, then cast onto a plastic mold, and allowed to dry in ambient conditions for 24 h. The dried PVA substrate was then carefully peeled off the mold; the resultant PVA films had thickness of 80 ± 5 μm. To fabricate electrodes, $Li_4Ti_5O_{12}$ (LTO) powder (MTI Corporation), Super P carbon (MTI Corporation), and PVA were mixed at weight ratio of 5:1:1 in DI water. The mixture was then stirred for 2 h to create a homogeneous slurry. Then, the slurry was printed on the PVA substrate at a thickness range of 24–40 μm to get prototypical electrodes of different thickness; or printed on an aluminum foil substrate to a thickness of 100 μm, dried and peeled off to obtain free-standing electrodes. A G25 (0.2 mm tip) precision gravity feed nozzle at constant pressure of 20 psi was used along with vinyl masks to spray-print the electrodes.

4.2. Mechanical Characterization of Electrode Layers

The nominal stress–strain curves for the free-standing electrodes were obtained using a dynamic mechanical analyzer (DMA) (Mettler Toledo, DMA-1). A tensile mode with force ranges from 0–0.15 N at the rate of 0.03 N min^{-1} was applied at room temperature. The sample is 10 mm in length, 2.5 mm in width, and 0.08 mm in thickness.

4.3. PVA Swelling Strain and Resultant Electrode Strain Measurements

Pristine PVA substrate and prototypical electrodes were immersed into water to measure the total strain in x-axis E11 of the electrode coating as a function of swelling strain. The prototypical electrode was immersed 2 s earlier than the pristine PVA substrate, to account for the delay in water penetration into the PVA substrate from the electrode coating side. The E11 of the electrode and the corresponding swelling strain of the PVA substrate was compared to the simulation result.

© 2017 WILEY-VCH Verlag GmbH & Co. KGaA, Weinheim

4.4. Characterization of Initial Defect Distribution, Crack Propagation, and Resultant Fragment Size

An optical microscope (AmScope) equipped with a charge-coupled device (CCD) was used to take images of the electrodes before, during, and after immersion. These images were used to obtain defect distribution, crack propagation, and fragment size, respectively. Images before and during immersion were taken with a 10× lens for high magnification, while images during and after immersion were taken by 4× lens to increase field of view. MATLABges during and after immersion were taken by 4 take images of the electrodes beto convert digital images to black-and-white images for further processing. White areas of the image were indicative of defects or cracking, while black areas represented more uniform, defect-free coating. Defect size and prevalence, as well as fragment size, were then determined from the monochrome images using MATLAB.

4.5. FEM Simulation

An FEM (finite element method) model was developed in ABAQUS to simulate substrate swelling in a substrate-electrode layered structure, and to predict the consequent strain on the electrode layer, as well as the initiation and propagation of cracks throughout the electrode layer. Two dimensional symmetry (about x- and y-axes) of the structures allows for simplification of the model to quarter symmetric. The PVA substrate and the electrode coating were connected by cohesive contact. The variation of the PVA substrate properties as a function of swelling strain[15] and true stress–strain curve of the electrode layer were applied for the analysis. A defect-free sample was assumed to obtain the strain of the electrode layer as a function of PVA swelling strain and verify the true stress–strain curve. An electrode layer with through-thickness defects was applied for simulation of crack initiation and propagation. The defect length ranged from 2.5 to 35 μm. The crack initiated when the max principle strain of the electrode layer reached 17%. Critical swelling strain (swelling strain at which crack starts to propagate) as a function of defect length was recorded.

Article first published online: xxxx
Manuscript Revised: March 16, 2017
Manuscript Received: February 16, 2017

[1] R. Montazami, C. M. Spillmann, J. Naciri, B. R. Ratna, *Sens. Actuators, A: Phys*. **2012**, *178*, 175.
[2] R. Zhang, Y. Chen, R. Montazami, *Materials* **2015**, *8*, 2735.
[3] J. L. Lu, W. S. Liu, H. Ling, J. H. Kong, G. Q. Ding, D. Zhou, X. H. Lu, *RSC Adv.* **2012**, *2*, 10537.
[4] W. Hong, A. Almomani, R. Montazami, *Measurement* **2017**, *95*, 128.
[5] S. Liu, R. Montazami, Y. Liu, V. Jain, M. Lin, J. R. Heflin, Q. M. Zhang, *Appl. Phys. Lett*. **2009**, *95*, 023505.
[6] M. D. Green, D. Wang, S. T. Hemp, J.-H. Choi, K. I. Winey, J. R. Heflin JR, T. E. Long, *Polymer* **2012**, *53*, 3677.
[7] C. Meis, N. Hashemi, R. Montazami, *J. Appl. Phys*. **2014**, *115*, 134302.
[8] K. S. Lee, S. Wuttiphan, X.-Z. Hu, S. K. Lee, B. R. Lawn, *J. Am. Ceram. Soc*. **1998**, *81*, 571.
[9] Y. W. Rhee, H. W. Kim, Y. Deng, B. R. Lawn, *J. Am. Ceram. Soc*. **2001**, *84*, 1066.
[10] J. Chen, S. Bull, *Thin Solid Films* **2009**, *517*, 3704.
[11] R. Jamshidi, Y. Chen, K. White, N. Moehring, R. Montazami, *MRS Adv.* **2016**, *1*, 2501.
[12] R. Jamshidi, S. Çinar, Y. Chen, N. Hashemi, R. Montazami, *J. Polym. Sci. Part B: Polym. Phys*. **2015**, *53*, 1603.
[13] S. Abrate, *Appl. Mech. Rev.* **1991**, *44*, 155.
[14] R. Darolia, *Int. Mater. Rev.* **2013**, *58*, 315.
[15] Y. Chen, R. Jamshidi, K. White, S. Çınar, E. Gallegos, N. Hashemi, *J Polym. Sci. Part B: Polym. Phys*. **2016**, *54*, 2021.
[16] T. Hao, X. Gong, Z. Suo, *J. Mech. Phy. Solids* **1996**, *44*, 23.
[17] A. J. Moulson, J. M. Herbert, *Electroceramics: Materials, Properties, Applications*, John Wiley & Sons, Chichester **2003**, p. 388.
[18] N. Lu, X. Wang, Z. Suo, J. Vlassak, *J. Mater. Res*. **2009**, *24*, 379.
[19] J.-Y. Sun, N. Lu, J. Yoon, K.-H. Oh, Z. Suo, J. J. Vlassak, *J. Appl. Phys*. **2012**, *111*, 013517.
[20] B. Choules, K. Kokini, *J. Eng. Mater. Technol*. **1996**, *118*, 522.
[21] S. Nusier, G. Newaz, *Eng. Fract. Mech*. **1998**, *60*, 577.
[22] K. Kokini, A. Banerjee, T. A. Taylor, *Mater. Sci. Eng. A* **2002**, *323*, 70.
[23] K. Kokini, J. De Jonge, S. Rangaraj, B. Beardsley, *Surf. Coat. Technol*. **2002**, *154*, 223.
[24] B. Zhou, K. Kokini, *Mater. Sci. Eng. A* **2003**, *348*, 271.
[25] S. Rangaraj, K. Kokini, *Acta Mater.* **2003**, *51*, 251.
[26] C. Chen, J. Pascual, F. Fischer, O. Kolednik, R. Danzer, *Acta Mater.* **2007**, *55*, 409.
[27] M. Rodriguez, N. Y. Shammas, *Microelectron. Reliab*. **2001**, *41*, 517.
[28] A. L. Young, G. E. Hilmas, S. C. Zhang, R. W. Schwartz, *J. Mater. Sci*. **2007**, *42*, 5613.
[29] C. J. Brennan, J. Nguyen, E. T. Yu, N. Lu, *Adv. Mater. Interfaces* **2015**, *2*, 1500176.
[30] N. A. Peppas, P. Colombo, *J. Controlled Release* **1989**, *10*, 245.
[31] T. Bussemer, N. Peppas, R. Bodmeier, *Eur. J. Pharma. Biopharm*. **2003**, *56*, 261.
[32] R. Wong, C. Tang, K. Chau, P. Lin, *Eng. Fract. Mech*. **2002**, *69*, 1853.
[33] B. Paliwal, K. Ramesh, *J. Mech. Phys. Solids* **2008**, *56*, 896.
[34] J. Yang, *J. Aircr.* **1980**, *17*, 528.
[35] J. Yang, *Proc. of 22nd Conf. of Structures, Structural Dynamics and Material*, American Institute for Aeronautics and Astronautics (AIAA), Atlanta **1981**, p. 38.
[36] P. White, L. Molent, S. Barter, *Int. J. Fatigue* **2005**, *27*, 752.
[37] L. Molent, Q. Sun, A. Green, *Fatigue Fract. Eng. Mater. Struct*. **2006**, *29*, 916.
[38] P. M. Moreira, P. F. de Matos, P. M. de Castro, Theor. *Appl. Fract. Mech*. **2005**, *43*, 89.
[39] Y. Liu, S. Mahadevan, *Int. J. Fatigue* **2009**, *31*, 476.

© 2017 WILEY-VCH Verlag GmbH & Co. KGaA, Weinheim

DOI: 10.1002/adem.201700139

[40] Y. Liu, S. Mahadevan, *49th AIAA/ASME/ASCE/AHS/ASC Structures, Structural Dynamics, and Materials Conf., 16th AIAA/ASME/AHS Adaptive Structures Conf., 10th AIAA Non-Deterministic Approaches Conf., 9th AIAA Gossamer Spacecraft Forum, 4th AIAA Multidisciplinary Design Optimization Specialists Conf*, American Institute for Aeronautics and Astronautics (AIAA), Schaumburg **2008**, p. 1761.

[41] V. Shenoy, K.-S. Kim, *J. Mech. Phys. Solids* **2003**, *51*, 2023.

[42] F. Zhou, J.-F. Molinari, K. Ramesh, *Int. J. Solids Struct.* **2005**, *42*, 5181.

[43] W. Drugan, *J. Mech. Phys. Solids* **2001**, *49*, 1181.

[44] Y. Chen, R. Jamshidi, W. Hong, R. Montazami, *Adv. Mater. Interfaces* **2017**, *4*, 1601076.

[45] M. Considère, Memoire sur l'emploi du fer et de l'acier dans les constructions: Dunod; **1885**.

[46] A. A. Griffith, Philos. *Trans. R. Soc. London Series A, Containing Papers Math. Phys. Charact.* **1921**, *221*, 163.

[47] R. Rivlin, A. G. Thomas, In Collected Papers of RS Rivlin, Springer, New York **1997**, 2615.

[48] A. Thomas, *Rubber Chem. Technol.* **1994**, *67*, 50.

DOI: 10.1002/adem.201700139
© 2017 WILEY-VCH Verlag GmbH & Co. KGaA, Weinheim